

All-optical spin access via a cavity-broadened optical transition in on-chip hybrid quantum photonics

Lukas Antoniuk^{1,†}, Niklas Lettner^{1,2,†}, Anna P. Ovvyan^{3,4,5}, Simon Haugg¹, Marco Klotz¹, Helge Gehring^{3,4,6}, Daniel Wendland^{3,4,6}, Viatcheslav N. Agafonov⁷, Wolfram H.P. Pernice^{3,4,5,6} and Alexander Kubanek^{1,2,*}

¹*Institute for Quantum Optics, Ulm University, Ulm 89081, Germany*

²*Center for Integrated Quantum Science and Technology (IQST), Ulm University, Albert-Einstein-Allee 11, Ulm 89081, Germany*


³*Institute of Physics and Center for Nanotechnology, University of Münster, Münster D-48149, Germany*

⁴*CeNTech — Center for Nanotechnology, Münster 48149, Germany*

⁵*Kirchhoff-Institute for Physics, Heidelberg University, Im Neuenheimer Feld 227, Heidelberg 69120, Germany*

⁶*SoN — Center for Soft Nanoscience, Münster 48149, Germany*

⁷*GREMAN, UMR 7347 CNRS, INSA-CVL, Tours University, Tours 37200, France*

 (Received 30 August 2023; revised 28 March 2024; accepted 12 April 2024; published 16 May 2024)

Hybrid quantum photonic systems connect classical photonics to the quantum world and promise to deliver efficient light-matter quantum interfaces while leveraging the advantages of both, the classical and the quantum, subsystems. However, combining efficient, scalable photonics and solid-state quantum systems with desirable optical and spin properties remains a formidable challenge. In particular, the access to individual spin states and coherent mapping to photons remains unsolved for hybrid systems. In this paper, we demonstrate all-optical initialization and readout of the electron spin of a negatively charged silicon-vacancy center in a nanodiamond coupled to a silicon nitride photonic crystal cavity. We characterize relevant parameters of the coupled emitter-cavity system and determine the silicon-vacancy center's spin-relaxation and spin-decoherence rate. Our results mark a key step towards the realization of a hybrid spin-photon interface based on silicon nitride photonics and the silicon-vacancy center's electron spin in nanodiamonds with potential use for quantum networks, quantum communication, and distributed quantum computation.

DOI: [10.1103/PhysRevApplied.21.054032](https://doi.org/10.1103/PhysRevApplied.21.054032)

I. INTRODUCTION

Quantum applications, such as quantum networks and quantum repeaters, rely on efficient mapping of quantum information between stationary qubits and flying qubits [1–3]. While photons are a natural choice for flying qubits, since they interact weakly with their environment [4], numerous candidates for stationary qubits are under investigation with individual strengths and weaknesses. The negatively charged silicon-vacancy (SiV⁻) center in diamond is of particular interest, since its defect symmetry enables excellent optical properties to be retained even in

nanodiamonds (NDs) with sizes below the optical wavelengths [5], recently enabling two-photon interference from SiV⁻ centers in remote NDs [6]. Hybrid quantum photonics [7,8] offers a unique route to efficiently interface stationary to flying qubits, by combining individually optimized photonic and quantum systems, therefore inheriting the advantages of each of its constituents. These hybrid systems can be assembled using pick and place transfer [9] or lithographic positioning [10] and can be categorized into evanescent [11,12] and embedded optical coupling strategies, where embedding the quantum system has reached high photonic enhancements in photonic crystal cavities (PCCs) and ring resonators [13,14]. However, until today access to stationary qubits was not demonstrated in coherent hybrid quantum photonics.

Here, we propose an ND-hosted SiV⁻ center's electron spin as a stationary qubit and experimentally demonstrate its access in hybrid quantum photonics entailing a number of advantages. The use of NDs is accompanied with a potential increase in the SiV⁻ center's electron-spin

*Corresponding author: alexander.kubanek@uni-ulm.de

†These authors contributed equally to this work.

Published by the American Physical Society under the terms of the [Creative Commons Attribution 4.0 International](https://creativecommons.org/licenses/by/4.0/) license. Further distribution of this work must maintain attribution to the author(s) and the published article's title, journal citation, and DOI.

coherence by a modification of the phonon density of states [15] or strain [16] in its environment. One-dimensional PCCs enable coherent and efficient exchange of quantum information between stationary qubits and flying qubits in the framework of cavity quantum electrodynamics (cQED) [17], while offering scalability by a small footprint on chip.

Our photonic base material is silicon nitride (Si_3N_4), which offers scalable fabrication and access to many key elements for quantum nodes integrated on a single chip [18]. The one-dimensional PCCs employed herein are formed in a single-mode Si_3N_4 waveguide on top of SiO_2 with periodic elliptical holes patterned into the waveguide. These periodic holes are interrupted by a hole defect at the midpoint of the waveguide, leading to localized modes within the guide, thus forming the cavity, while this hole defect also serves as a target region for ND placement. At this point, another single-mode Si_3N_4 waveguide crosses the cavity waveguide orthogonally, with waveguide dimensions optimized for off-resonant excitation of the SiV^- centers. Each of the two waveguides are equipped with efficient broadband out-of-plane couplers [19] to interface the nanostructure with Gaussian optics. Further details on the photonic device are provided in Appendix B.

II. HYBRID DEVICE ASSEMBLY

Start of the assembly of our hybrid emitter-cavity system is identifying suitable SiV^- center hosting NDs at room temperature via confocal microscopy. The procedure and ND synthesis is described in Appendix C. Suitable candidates are transferred to the PCC by AFM pick and place, following the method in Ref. [13]. In order to overcome limitations of evanescent coupling on top of the waveguide, the ND of choice [Fig. 1(a)] is placed inside a PCC hole [Fig. 1(b)] close to the cavity center [see Appendix D]. After transfer the ND is well embedded, as verified by its AFM height cross section [Fig. 1(b), inset]. The whole ND assembly does not negatively affect the cavity properties, which we probe utilizing the Si_3N_4 inherent background fluorescence and the broadband out-of-plane couplers. A green laser is directed onto one of the cavity couplers and excites Si_3N_4 background fluorescence, which is modulated by the cavity when collected at the opposing coupler [Fig. 1(c)]. After the assembly the quality factor Q of the resonance mode closest to 737 nm is determined to be $Q = 1015(19)$, while the resonance position is nearly unchanged [Fig. 1(d)]. A quantitative analysis and additional details of the assembly are presented in Appendix D.

Successful placement of SiV^- centers is verified at cryogenic temperatures (approximately 4K) by off-resonant excitation via the pump waveguide and fluorescence collection at one of the cavity couplers [Fig. 1(e)] revealing cavity channeled SiV^- center fluorescence [Fig. 1(f)]. Alternatively a scanable titanium-sapphire laser is coupled

into the cavity and fluorescence is detected from the SiV^- center phonon sideband at the cavity center in a photoluminescence excitation (PLE) experiment [Fig. 1(g)]. An exemplary measurement is seen in Fig. 1(h) revealing multiple peaks, corresponding to the laser hitting resonance with strain-shifted SiV^- centers in the ND. Strain alters the SiV^- center's ground- (Δ_{GS}) and excited-state (Δ_{ES}) splitting [Fig. 2(a)] as well as the weighted central wavelength (zero phonon line) of the optical transitions $A-D$ [5,20], which allows us to address individual SiV^- centers.

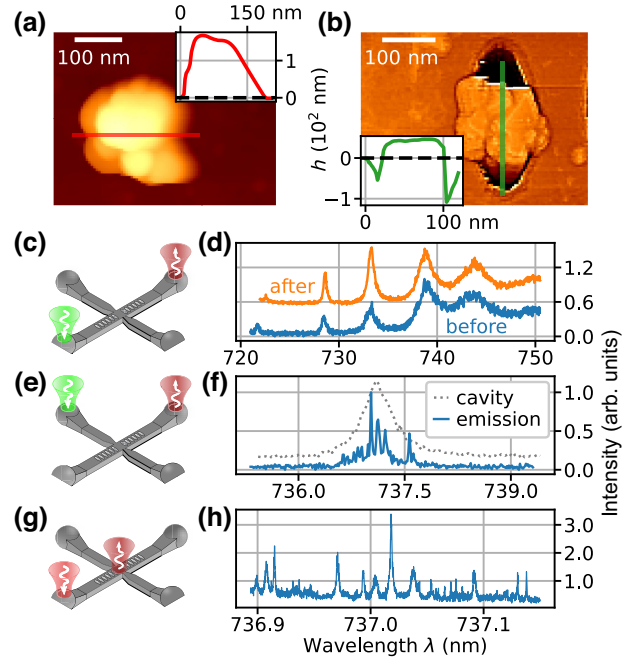


FIG. 1. (a) Atomic force microscope (AFM) scan and height profile (inset) of the SiV^- center hosting NDs on a fused silica substrate. (b) Parts of the same ND embedded inside the first hole from the PCC's center. The data is filtered with an unsharpen mask and the green line indicates the height profile path along the unfiltered data (inset). (c) Measurement scheme to spectrally resolve the cavity resonance wavelengths by exciting broadband Si_3N_4 fluorescence, which gets modulated by the cavity. (d) Normalized cavity spectrum before (blue) and after (orange, offset by 0.5) the pick and place procedure. Data is measured as sketched in (c). (e) Measurement scheme to detect cavity channeled SiV^- center fluorescence via off-resonant excitation over the crossed waveguide. (f) Cavity channeled SiV^- center fluorescence (blue, data normalized) at cryogenic temperatures, measured as sketched in (e), with the cavity tuned into resonance. This is indicated by the normalized and offset cavity spectrum (dashed gray). (g) Resonant excitation scheme with the laser coupled into the cavity via a coupler and fluorescence detection at the PCC's center within the SiV^- center phonon sideband. Details for this measurement type are found in Appendix L. (h) Using the scheme presented in (g) and tuning the excitation laser frequency reveals distinct peaks signaling resonance with the successfully placed SiV^- centers.

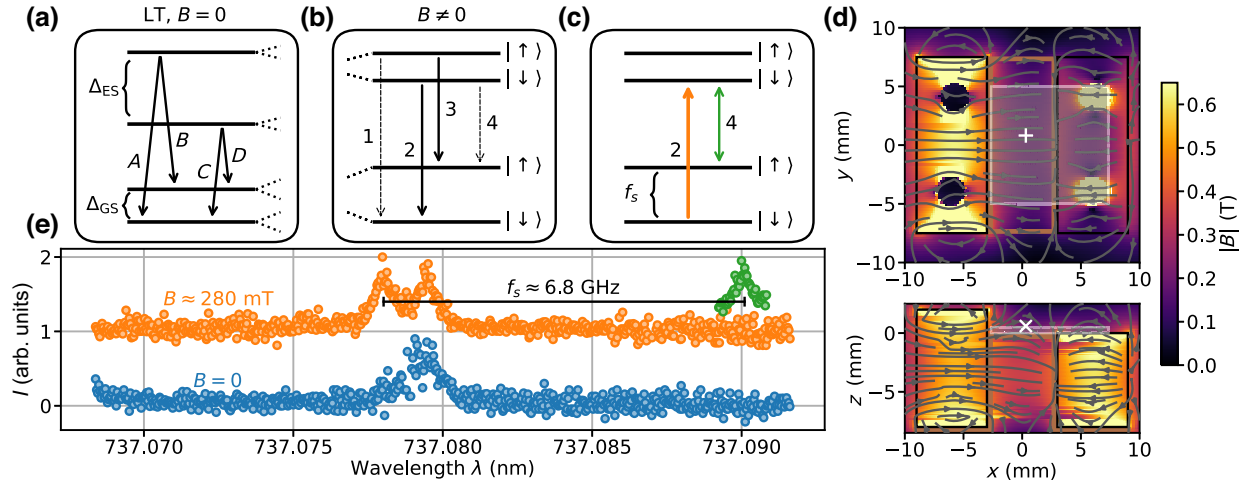


FIG. 2. (a) Level scheme of an SiV^- center at cryogenic temperatures with four optical transitions, labeled A to D , connecting spin degenerate spin-orbit eigenstates separated by the strain-dependent ground- (Δ_{GS}) and excited-state splitting (Δ_{ES}). (b) In a magnetic field the level's spin degeneracy is lifted resulting in four transitions (1–4) per level and enables optical access to the spin degree of freedom. (c) Measurement scheme to probe the spin flipping transition 4. Continuous pumping on transition 2 (orange arrow) and probing for transition 4 (green arrow) with a second laser enables the splitting f_s of the spin states to be determined. (d) Simulation of the magnetic field from two permanent magnets (black rectangles), which are screwed to the sides of the coldfinger (copper colored lines), onto which the photonic chip (gray square) is mounted. White crosses mark the position of the PCC. Simulations were performed using MAGPYLIB [21]. (e) Optical SiV^- center transitions seen in a cavity PLE scan (blue) can split up when a magnetic field is applied (orange) due to a difference in spin splitting in the ground and excited state. Pumping one of the spin-preserving transitions, and probing with a second laser reveals the spin-flipping transition (green). Data is normalized and offset.

III. SPIN ACCESS

The SiV^- center's spin-orbit eigenstates, connected by these optical transitions, are spin degenerate in zero magnetic field [22–24]. In a static magnetic field each eigenstate splits up due to the spin-1/2 nature of the SiV^- center. The resulting spin sublevels are denoted $|\downarrow\rangle$ and $|\uparrow\rangle$ herein [Fig. 2(b)]. Transitions between these states are labeled 1–4 in Fig. 2(b) and are apparent for each of the optical transitions A – D . Here, the magnetic field is generated by a permanent neodymium magnet assembly, with simulated field strength above 250 mT [Fig. 2(d)]. The largest field component lies along the x axis at the location of the PCC [see Appendix F], which ensures that the magnetic field is parallel to well-coupled SiV^- centers with their dipole axis parallel to the transverse-electric (TE) cavity mode. Alignment of the magnetic field to the SiV^- center symmetry axis improves parameters, such as the spin-state purity [22] and the spin relaxation time, which influences the cyclicity of the optical transitions [25]. Transition 2 and 3 potentially possess long cyclicity and connect levels of equal spin projection, hence also referred to as *spin-preserving* transitions, while for transition 1 and 4 the spin will be flipped (*spin flipping*). The spin splitting in the ground and excited state depends on the spin as well as the orbital degree of freedom, where the latter is larger in the excited state [22]. Consequently, transition 2 and 3 are spectrally separated, enabling all-optical electron spin access [24].

The intensity ratio of spin-flipping and spin-preserving transitions depends on the magnetic field alignment relative to the symmetry axis of the SiV^- center, with the spin-flipping transition intensity being minimized for parallel alignment [24]. Here, a nonvanishing out of plane component of the magnetic field [Appendix F] and an angle of the SiV^- center with respect to the TE mode of the cavity [Appendix I] leads to weakly allowed spin-flipping transitions, with a nonvanishing dipole overlap with the cavity field. In this case [Fig. 2(e)] one can probe and reveal the spin-flipping transition by continuously driving one of the spin-preserving transitions while sweeping a second laser's frequency [Fig. 2(c)]. The respective frequency difference yields the spin splitting $f_s \approx 6.8$ GHz, which translates to approximately 280 mT, which is in the expected range from the magnetic field simulations of Fig. 2(d).

IV. EMITTER-CAVITY SYSTEM

To determine the relevant cQED parameter set $\{g, \kappa, \gamma\}$, with the single-photon Rabi frequency g , the cavity decay rate κ , and the transition linewidth γ , the linewidth for both spin-preserving transitions is measured at varying probe intensities on and off resonant with the cavity resonance [Fig. 3]. Extrapolating to zero power according to $\gamma = \gamma_0 \sqrt{1 + P/P_{\text{sat}}}$ [26] mitigates any influence of power broadening. Tuning the cavity resonance frequency

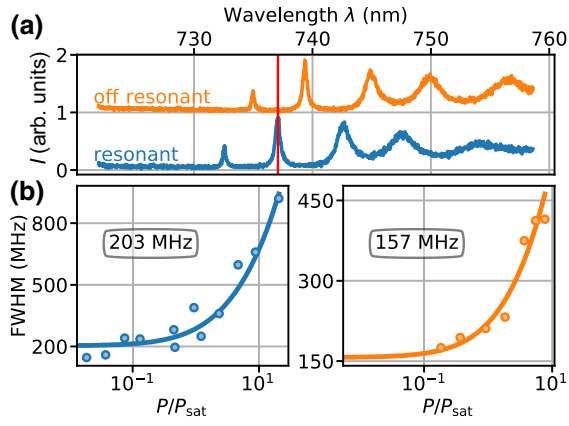


FIG. 3. (a) Cavity spectrum on (blue) and off resonance (orange) with the SiV^- center, measured as sketched in Fig. 1(c). The vertical red line coincides with the corresponding transition wavelength. (b) Power-dependent PLE linewidth of the two spin-preserving transitions on (blue) and off resonance (orange) with the cavity for the SiV^- center discussed in Fig. 2. The measurement scheme follows Fig. 1(g).

is realized by controlled freezing of N_2 to the PCC [27], shifting the cavity resonances to longer wavelengths. Extracting γ from the extrapolated zero power value yields $\gamma/2\pi = 157(25)$ MHz at a cavity detuning of $\Delta \approx 5\kappa$ [Fig. 3, orange]. This value is consistent with the Fourier-transform limit of the SiV^- center in NDs, where lifetimes

in the range from 200 ps to 2 ns had been observed at room temperature [28]. The cavity decay rate κ is determined by the Lorentzian line shape of the resonance resulting in $\kappa/2\pi = 273(7)$ GHz, which was positively affected by the gas tuning, as discussed in Appendix K. From the zero power extrapolated Purcell broadened linewidth $\gamma_{\text{on}}/2\pi = 203(23)$ MHz [Fig. 3(b), orange] measured with the cavity in resonance ($\Delta = 0.042(7) \cdot \kappa$) [Fig. 3(a), blue], we can infer the cooperativity C [29] to be $C = 0.30(24) = \frac{4g^2}{\kappa\gamma}$ translating to $g/2\pi = 1.8(13)$ GHz for the spin-preserving transitions. The complete cQED parameter set reads

$$\{g, \kappa, \gamma\}/2\pi = \{1.8, 273, 0.157\} \text{ GHz.}$$

V. SPIN PROPERTIES

All-optical spin access is realized by optical pumping on one of the spin-preserving transitions [Fig. 4(a)], starting from equal population in $|\downarrow\rangle$ and $|\uparrow\rangle$ in thermal equilibrium at 4 K and a spin splitting of $f_s \approx 6.8$ GHz. During a 1- μs -long laser pulse [Fig. 4(b), right], this thermal equilibrium is disturbed by laser-induced optical spin pumping via the spin-flipping transition, depopulating the level $|\downarrow\rangle$. The fluorescence in the phonon sideband, probed in accordance to Fig. 1(g), exponentially decays on a timescale of approximately equal to 70 ns, corresponding to the spin initialization time. The steady state reached towards the end of the laser pulse yields a final population in the spin-state

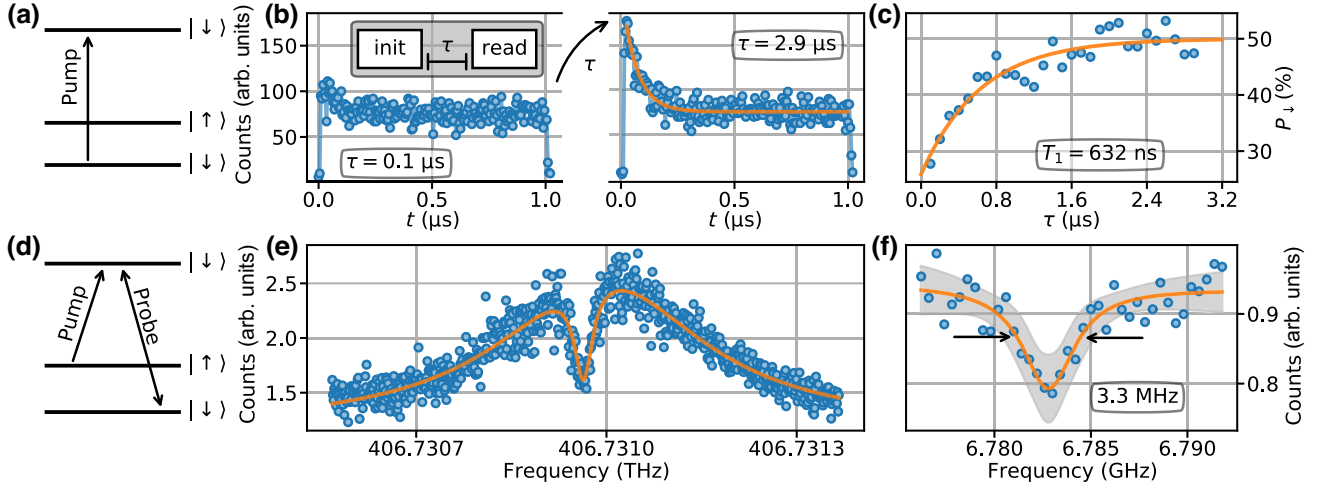


FIG. 4. (a) Measurement scheme to probe the spin relaxation time T_1 of the SiV^- center. A laser resonant with transition 2 (see Fig. 2) depopulates the $|\downarrow\rangle$ level and pumps population to $|\uparrow\rangle$. (b) Time-resolved fluorescence during the laser pulse. Increasing the pulse separation τ between consecutive laser pulses leads to increased fluorescence at the start of the laser pulse, due to exponential recovery towards thermal equilibrium during τ . Fitting (orange, right-hand panel) yields the spin initialization timescale of approximately equal to 70 ns (c) Exponential recovery of population to thermal equilibrium versus laser pulse spacing τ . The recovery timescale yields $T_1 = 630(130)$ ns. (d) coherent population trapping (CPT) experiment to extract the spin-dephasing rate Γ_2^* . One laser fixed in resonance with, e.g., transition 4 while another laser is scanned across the corresponding transition forming a Λ -type system. (e) Sweeping the probe laser frequency yields the characteristic dip in the fluorescence signal as the system is trapped in the coherent superposition. (f) Probing this dip width at low excitation powers and phase coherent electro optical modulator (EOM) generated side bands reveals a minimum dip width of 3.3(7) MHz. Gray shaded area is the fit's 3σ confidence band.

$|\uparrow\rangle$ with a fidelity of approximately equal to 75%, extracted from $1 - h(0)/2h(\tau \rightarrow \infty)$, with h being the peak height at the leading edge. By applying consecutive laser pulses with a varying interpulse delay, the characteristic relaxation time for the spin-state T_1 can be retrieved from an exponential fit of the corresponding initial peak heights [Fig. 4(c)], which yields $T_1 = 630(130)$ ns. T_1 is typically limited due to nonperfect alignment of the SiV^- center symmetry axis and the magnetic field, which in our case indicates potential improvement in the coupling strength to the PCC. As outlined earlier, ideally the magnetic field, the SiV^- center symmetry axes and the TE mode are colinear. However, in the given configuration we attribute a decreased T_1 to a nonzero z component of the magnetic field and dipole misalignment to the cavity, discussed in Appendices F and I, respectively. With vector control of the magnetic field, the misalignment could be determined and optimized by means of AFM nanomanipulation [30]. In addition to the spin-relaxation time T_1 , the dephasing rate Γ_2^* is of key interest, being the timescale dictating operations on the electron spin. To probe Γ_2^* , a coherent population trapping (CPT) experiment is carried out where two laser fields are simultaneously applied to the SiV^- center connecting a spin-preserving and spin-flipping transition in a Λ -type system [Fig. 4(d)]. When both lasers fulfill the Raman condition at zero detuning a coherent dark state is formed leading to a dip in fluorescence signal [Fig. 4(e)]. The dip width is a direct measure of Γ_2^* [24] when ensuring phase coherence of the laser fields and excluding powerbroadening. This is realized by generating sidebands through microwave drive of an EOM and minimizing the excitation power. The dip width was measured to be as narrow as $\Gamma_2^* = 3.3(7)$ MHz [Fig. 4(f)], which translates to $T_2^* = 1/(\pi\Gamma_2^*) = 97(20)$ ns in this low-power regime [see Appendix J].

VI. CONCLUSION

In conclusion, we demonstrate the fundamental step for an on-chip hybrid spin-photon interface based on the electron spin of a SiV^- center in NDs and Si_3N_4 photonics. We achieve a cooperativity of $C = 0.30(24)$ and single-photon Rabi frequency of $g/2\pi = 1.8(13)$ GHz, which both could be further improved by increasing the ratio of Q factor to mode volume V . The simultaneous requirements set herein for spin access and proper optical coupling to the PCC restricts us to a small number of SiV^- centers within the ND. Using a higher density of SiV^- centers or decreasing the crystal strain, which has direct influence on the possibility for optical spin access [20], could increase the number of SiV^- center candidates fulfilling both criteria. A further boost in coupling can be envisioned with additional alterations in the cavity design, targeting parameters, such as scattering-induced internal losses, which are discussed in Appendix E, or additional

optimization through nanomanipulation steps [30,31] for dipole alignment. With the above turning knobs at hand, cooperativities well above one are within close reach. The accomplished spin initialization fidelity of approximately equal to 75% and the spin-relaxation time T_1 of 630(130) ns of our cavity coupled SiV^- center could be improved by alignment of the magnetic field to the SiV^- center symmetry axis through vector control. This should increase the spin relaxation time T_1 to orders of ms [24,32] and enables long cyclicity of the spin-preserving transitions giving access to single-shot readout [33], while also increasing the upper bound for the spin coherence time T_2 . The measured spin-dephasing rate of $\Gamma_2^* = 3.3(7)$ MHz is in the range of values obtained for bulk diamond by optically detected magnetic resonance at approximately 2 K in a bath cryostat [32], suggesting the feasibility of integrating SiV^- centers in NDs with potentially improved spin properties [15], with dephasing rates recently surpassing SiV^- centers in bulk by an order of magnitude [34]. Implementation of on-chip microwave structures to coherently control the electron spin, or techniques relying on all optical driving [35,36], together with the above-mentioned improvements leading to cooperativities well above one could enable spin-photon entangling gates based on spin-dependent cavity reflection signal [37,38].

ACKNOWLEDGMENTS

The project was funded by the BMBF/VDI in Project HybridQToken. A.K. acknowledges support of the Baden-Wuerttemberg Stiftung gGmbH in Project No. BWST-ISF2018-008. The AFM was funded by the DFG, we thank Professor Kay Gottschalk for the support. N.L. acknowledges support of the IQST. The authors thank V.A. Davydov for synthesis and processing of the nanodiamond material, and P. Maier for production of the FIB markers. D.W. acknowledges funding from the Deutsche Forschungsgemeinschaft (CRC 1459). H.G. acknowledges financial support of the Studienstiftung des deutschen Volkes. Experiments have been orchestrated by the open-source software Qudi [39].

APPENDIX A: EXPERIMENTAL SETUP

The optical setup is build around a dual-axis galvo scanning mirror (Thorlabs GVS212/M) and two $f = 300$ mm lenses. In contrast to a standard confocal microscope based on such a configuration, the galvo is bypassed with the help of a pellicle beam splitter (BP208). This way, the excitation laser spot can be fixed on the sample, while fluorescence can be collected from a different location [Fig. 5, red solid path] with the objective (Olympus LMPlanFl 50X/0.50), while spatial filtering is ensured by a 50- μm core multimode fiber. Position scanning of the whole cryostat (Janis ST-500) enables the excitation laser to be moved to the correct position. For excitation,

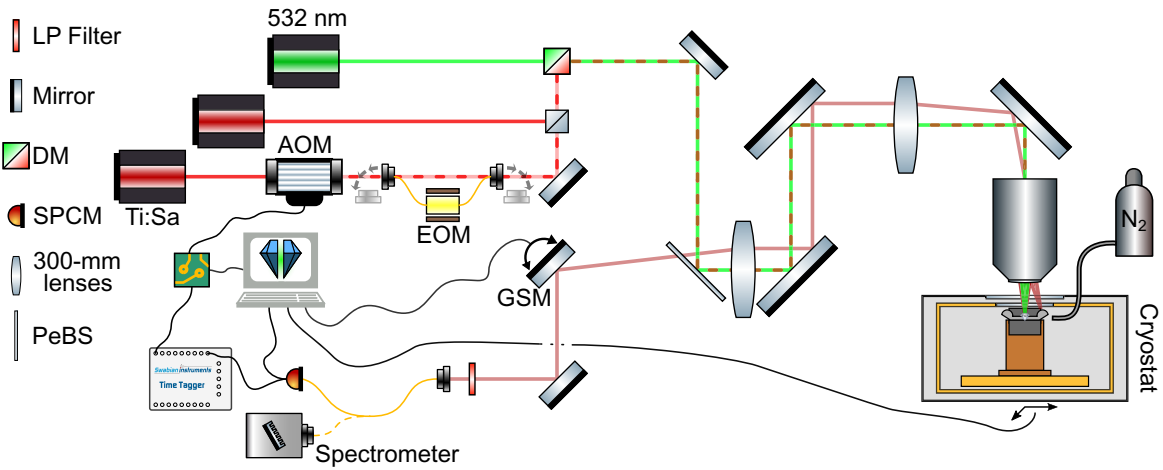


FIG. 5. Sketch of the experimental setup used for the measurements presented above. An off-resonant green laser and two titanium-sapphire (Ti:Sa) lasers can be directed towards the cryostat after being reflected off a pellicle beam splitter (PeBS). One of the Ti:Sa lasers can be modulated by an acousto-optic (AOM) or electro-optical modulator (EOM). The excitation light is focused onto the photonic chip in the cryostat with an objective. Fluorescence from a different location than the excitation spot can be collected using a galvo scanning mirror (GSM) and a 50- μm core multimode fiber, acting as a pinhole. The fiber-coupled photons are either recorded using a single-photon-counting module (SPCM), or spectrally resolved on a spectrometer. The electrical signal of the SPCM is either recorded as time tags for pulsed experiments or the count rate serves as feedback for position optimization of laser positioning as well as detection optimization with the GSM.

two types of lasers are utilized herein. A 532-nm laser (gem 532) and two tunable titanium-sapphire (Matisse 2 TS) lasers. The 532-nm laser is used for off-resonant excitation of SiV^- centers and to excite the broadband cavity background fluorescence with which the cavity parameters can be probed. The tunable titanium-sapphire lasers are used in the resonant PLE and CPT experiments. One of these laser beam paths is equipped with an acousto-optic modulator (G&H 3550-199), used for active excitation power stabilization and to generate the pulses for the T_1 measurement in Sec. V. For the CPT experiment, an additional electro-optical modulator (Jenoptik AM705b) is added to this path, which generates the phase coherent sidebands when driven by a continuous-wave microwave source (SMIQ06B). The electro-optical modulator is stabilized to its interferometric working point with a lock-in and a PID controller (DLC pro laser driver). Triggers and experiment timing is provided by an in-house programmed FPGA (XEM6310-LX45) and time traces are recorded with a time tagger (Swabian Instruments TimeTagger Ultra) for pulsed experiments. For resonant experiments, fluorescence is collected in the phonon sideband region of the SiV^- centers using bandpass fluorescence filters (2x Semrock 769/41), while for the off-resonant excitation experiments a 600-nm longpass filter blocks out the green excitation laser. Fluorescence is spectrally resolved with a spectrometer (Princeton Instruments HRS 500) equipped with gratings of 1200 grooves/mm, 750 nm blaze and 1800 grooves/mm, 670 nm blaze. Positioning of the sample and galvo scanning mirror, as well as

acquisition of photon counts from the single-photon-counting module (Excelitas SPCM-AQRH-14-FC) is done with a National Instruments data-acquisition card (PCIe-6323) and the open-source software qudi [39]. To introduce the N_2 gas into the cryostat an ultrahigh vacuum gas-dosing valve (Nenion F3VCR-012) controls flow through a 1/16 in. stainless steel tubing (Swagelok), which is directly facing the PCC chip inside the cryostat.

APPENDIX B: PHOTONIC DEVICE DETAILS

The crossed bar PCC is formed by two identical nonuniform Bragg mirrors, each consisting of N segments of elliptical holes at a period a , as sketched in Fig. 6. The ellipticity is characterized by a ratio of 2.5 of major axis c to minor axis d , optimized by three-dimensional Finite Difference Time Domain (FDTD) simulations to maximize the Q factor of the PCC. These elliptical holes ensure a

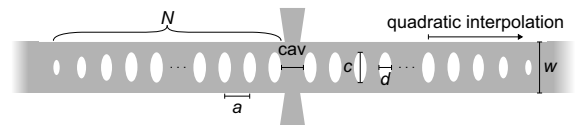


FIG. 6. Sketch of a PCC in a single-mode waveguide of width w . The PCC is characterized by the number of mirror segments N , the period a , and the defect distance cav . Towards the end of the mirror, the holes are quadratically interpolated, to ensure a smooth transition into the waveguide mode.

TABLE I. Parameters of the PCC considered in the main text.

N	a	cav	c/d	ff
45	240 nm	210 nm	2.5	0.24

wider band gap and higher reflectivity leading to stronger confinement of the optical mode in comparison to simple round-shaped holes, as employed in Refs. [11,13]. The mirror segments in each Bragg mirror are characterized via quadratically interpolated filling fraction of each segment $ff = (\pi cd/4wa)$ resulting in a smooth transition of the resonance mode into the waveguide mode. The width w (500 nm) and the thickness (200 nm) of the Si_3N_4 layer ensure single-mode fundamental TE mode guidance in the cavity waveguide. Notably, the demonstrated PCC devices on SiO_2 utilized herein are more robust and easier to fabricate in comparison to their suspended counterparts, as employed in Refs. [11,13], which rely on complex nanofabrication techniques. The broadband out-of-plane couplers, which interface the planar integrated waveguides are fabricated by direct laser writing using the *Nanoscribe GT* system. The couplers are connected to the Si_3N_4 photonics by an inverse Si_3N_4 taper, which couples the mode out of the waveguide into a mode converter. This allows for adiabatic conversion from waveguide modes to the ones guided in the polymer. To enlarge the mode, a linear polymer taper is attached and terminated by a reflection surface that directs the light upwards through total internal reflection. Afterwards, the waveguide is met by a convex lens, which focuses the light above the coupler [19]. Furthermore, to suppress unwanted fluorescence from the used polymer, all structures are printed with a mixture of IP-Dip NPI and a small fraction of Irgacure 819 as described in Refs. [40,41]. The PCC considered in the main text is characterized by the parameters summarized in Table I.

APPENDIX C: NANODIAMOND SYNTHESIS AND CHARACTERIZATION

The NDs with SiV^- centers used in this work were synthesized using a high-pressure high-temperature (HPHT) process without metal catalysts. The starting reagent for the synthesis was the mixture of naphthalene (C_{10}H_8) and tetrakis(trimethylsilyl)silane ($\text{C}_{12}\text{H}_{36}\text{Si}_5$). The experimental procedure consisted of loading the high-pressure apparatus to 8.0 GPa, heating the samples with reagent up to 1450 °C with short (3 s) isothermal exposures. Afterwards the recovered sample was treated with a mixture of concentrated $\text{HNO}_3 + \text{HClO}_4 + \text{H}_2\text{SO}_4$ acids to remove sp^2 carbon, as well as with HF acid to remove excess silicon. The obtained ND crystals were washed and dried. In preparation for optical characterization, the NDs are dispersed in ethanol, ultrasonicated, and drop casted onto a

150- μm fused silica coverslip into which marker structures had been fabricated by focused ion beam milling. Suitable SiV^- center hosting NDs are searched with a home-built confocal microscope, equipped with a 1.35-NA oil objective. The markers on the substrate serve as position reference, in order to relocate specific SiV^- center containing NDs in AFM measurements prior to the pick and place transfer.

APPENDIX D: HYBRID DEVICE ASSEMBLY

During the pick and place transfer of the ND of choice, seen in Fig. 7(a), the ND declustered and multiple particles were found in the subsequent AFM scan of Fig. 7(b) on top of the cavity. To avoid limitations from evanescent coupling on top of the waveguide, the parts, which had not been directly successfully placed into the cavity hole, were moved into their next-nearest cavity hole [Fig. 7(c)]. Remarkably, even though multiple cavity holes had been equipped with NDs the cavity parameters remain stable, also over the course of the additional experiment duration which in total added up to more than 2 years.

A detailed comparison, before and after the placement is given in Fig. 7, for the first, second, and third mode of the PCC. The spectra are measured in accordance with the sketch in Fig. 1(c). The quality factor Q of the first mode increased from 2100(400) to 4700(900), for the second mode from 1440(110) to 2020(50) and for the third mode from 680(40) to 1015(19) after the ND placement. However, due to a long time difference of approximately 1.5 years between the two spectra measurements, we refrain from assigning this increase solely to the placement of the ND, even though this is partially suggested by the supporting simulations in the Appendix E. With regards to

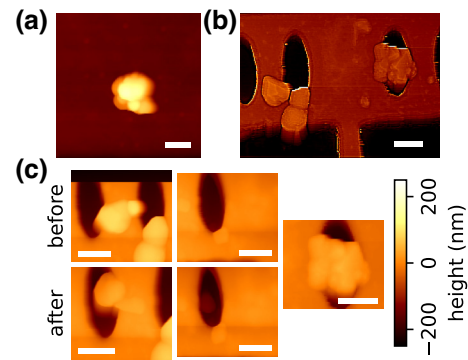


FIG. 7. (a) Uncut AFM image of the ND on the fused silica substrate. (b) AFM image after the pick and place procedure. The image is processed with an unsharpen mask. Parts of the ND were directly placed into a cavity hole, yet some other fractions remained on top of the cavity waveguide. (c) AFM images before (top) and after (bottom) a nanomanipulation step, which moved the remains [Fig. 7(b)] on top of the cavity waveguide into the closest PCC holes. Scalebars indicate 100 nm.

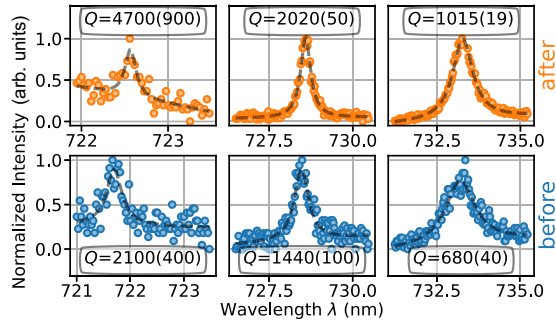


FIG. 8. Quality factors of the PCC before (blue) and after (orange) the ND insertion of the data in Fig. 1(d), for the first (left panel), second (middle panel), and third mode (right panel) with indications of an increasing Q factor upon ND placement. Due to the long time of approximately 1.5 years between these measurements we do not assign this increase in all of its extent to the ND placement.

spectral shifts Δ_i ; $i \in \{1, 2, 3\}$ the first mode is affected the most with a shift of $\Delta_1 = 0.867(18)$ nm. The second mode shifted by $\Delta_2 = 0.128(1)$ nm, while for the third mode the shift is determined to be $\Delta_3 = 0.065(16)$ nm. As long as the cavity mode of interest stays blue detuned from the target wavelength within a range of roughly 10 nm the mode can be tuned into resonance by gas tuning.

APPENDIX E: SIMULATIONS OF THE CAVITY AND HYBRID SYSTEM

To investigate the influence of ND placement, FDTD simulations of the hybrid PCC-ND system are carried out using the software MEEP [42] for three cases. Case 1 [Fig. 9(a)] represents the bare PCC characterized by the parameters in Table I. For case 2 [Fig. 9(b)] an ND is completely filling up the first hole besides the hole defect in the center of the PCC. In case 3 [Fig. 9(c)] the ND is only partially filling up the same hole, which closely matches the experimental configuration. The ND dimension [see Fig. 1(a)] on the bare substrate is approximately equal to 150 nm^3 , while after placement [Fig. 1(b)] it sticks out approximately equal to 40 nm from the cavity waveguide surface. The simulated results of Q factor and resonance wavelength λ for the first three modes, whose mode profile is sketched in Fig. 9(e), are summarized in Table II.

The simulations reveal a decrease in Q factor upon completely filling the cavity hole, as well as a red shift of the resonances, while the Q -factor drop is more significant for the second mode. However, the partial embedding of the ND in case 3 can induce a positive effect, leading to an increase in Q factor for the first mode, while the third mode almost maintains its value. Hence, parts of the increase seen in Fig. 8 could originate from the ND placement. This increase could be explained by the ND effectively creating a hole taper towards the hole defect, which, similar to the

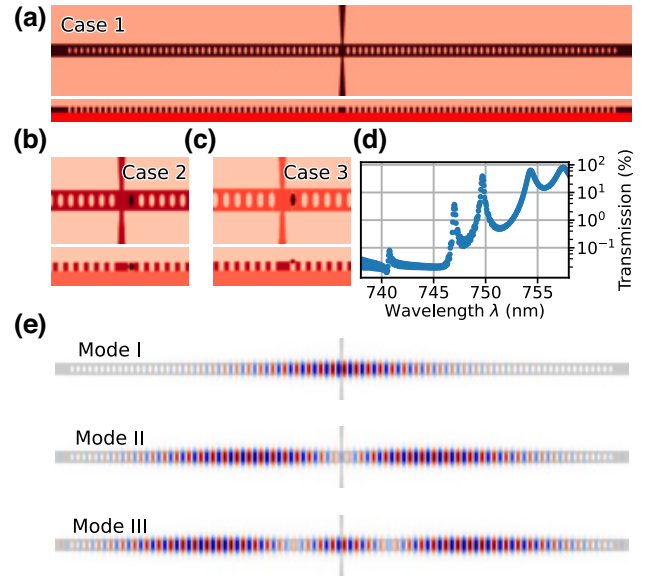


FIG. 9. (a) PCC geometry considered in the simulations for case 1, the bare cavity without an ND, in top view (upper panel) and cross-section view (bottom panel). (b) Enlarged top view (upper panel) and cross-section view (lower panel) of case 2 for the simulations, with an ND filling up the first hole besides the centered hole defect region of the PCC. (c) Case 3 of the simulations in an enlarged top view (upper panel) and cross-section view (lower panel), where the ND is only partially filling up the same PCC hole as for case 2. (d) Simulated transmission spectrum of the PCC in order to quantify the losses in the system. (e) Electric field distribution of the first three modes of the PCC, which are investigated in the three cases of the simulations.

quadratic taper at the end of the hole pattern in the cavity waveguide, ensures a smoother transition, which reduces scattering losses. All modes experience a less pronounced red shift in comparison to case 2, with a red shift also being present in the experimental comparison. The global offset in resonance wavelength between experiment and simulation is assigned to originate from strain in the Si_3N_4 after fabrication, decreasing the mean refractive index therefore blue shifting the resonances [43]. The relative offsets

TABLE II. Simulation results for the resonance wavelength λ and quality factor Q of the bare PCC (case 1), the PCC with a completely filled hole (case 2) and for a partially filled hole (case 3) as sketched in Figs. 9(a)–9(c).

	Case 1	Case 2	Case 3
Mode I	$\lambda = 740.69$ nm $Q = 5564$	$\lambda = 742.22$ nm $Q = 5138$	$\lambda = 741.19$ nm $Q = 6463$
Mode II	$\lambda = 746.98$ nm $Q = 6754$	$\lambda = 747.13$ nm $Q = 3687$	$\lambda = 747.03$ nm $Q = 4751$
Mode III	$\lambda = 749.69$ nm $Q = 4406$	$\lambda = 750.11$ nm $Q = 3757$	$\lambda = 749.77$ nm $Q = 4360$

are consistent for different chips fabricated from the same wafer.

To gain insights on the cavity losses, the transmission efficiency of the empty device is simulated [Fig. 9(d)], where the transmission T is given by $T = Q_{tot}^2 / Q_{wg}^2 = \kappa_{wg}^2 / (\kappa_{wg} + \kappa_{sc})^2$, with the cavity internal scattering losses κ_{sc} and guided decay κ_{wg} . For the third mode, which is used in the experiment, the transmission efficiency is simulated to be $T \approx 40\%$. However, in the experimental data decreases in scattering losses are apparent during the gas-tuning process, indicated by an increasing Q factor, as discussed in Appendix K.

APPENDIX F: MAGNETIC FIELD COMPONENTS

To supply the magnetic field, two permanent neodymium magnets are enclosing the coldfinger such that the photonic chip can still be mounted on the copper of the coldfinger in order to ensure proper cooling [Fig. 2(e)]. An asymmetric magnet configuration is chosen, which yields a higher overall field strength at the location of the PCC as well as a higher x component along the cavity axis, in comparison to a symmetric magnet configuration, which is flush with the surface of the coldfinger. The field components of the asymmetric configuration and the resulting out-of-plane angle is presented in Fig. 10 and is simulated using MAGPYLIB [21].

APPENDIX G: TRANSITION SHIFTS

Investigations on the SiV^- center discussed in the main text were carried out over the course of approximately 8 months and the data presented had been acquired during multiple cool-down cycles. During these temperature cycles the change in strain environment does lead to some variations in transition frequency of the SiV^- centers, yet

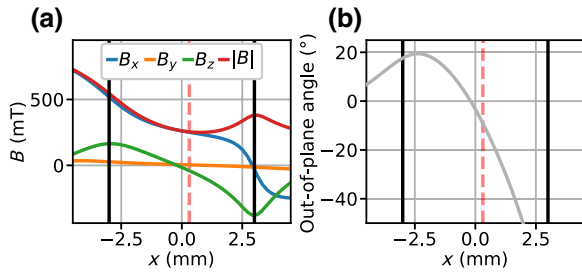


FIG. 10. (a) Vector components B_x, B_y, B_z (blue, orange, green) and magnitude $|B|$ (red) of the magnetic field of the magnet assembly [Fig. 2(e)] versus x position. The location of the PCC of interest and hence the SiV^- centers is marked by the dashed red line. The corners of the magnets are marked by the vertical black lines. (b) Out-of-plane angle of the magnetic field as a function of x position of the magnet assembly. The location of the PCC of interest and at the SiV^- centers is marked by the dashed red line. The corners of the magnets are represented by the vertical black lines.

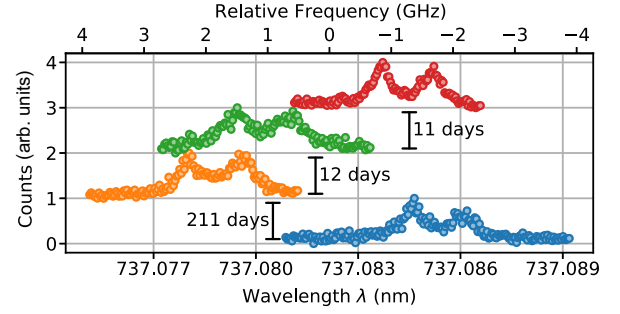


FIG. 11. Transition frequency variation over different cool-down cycles for the SiV^- center discussed in the main text. The data is normalized and offset for visibility purposes and the time difference between the data is annotated.

for the specific SiV^- center considered in the main text, this variation stayed within a window of approximately 6 GHz (Fig. 11). Parameters, such as the spin-relaxation time or the spin splitting, were used to uniquely identify and discriminate the corresponding SiV^- center.

APPENDIX H: CAVITY BACKGROUND TRANSMISSION METHOD VERSUS RESONANT TRANSMISSION

Probing a cavity for its resonance position is usually done by monitoring the transmission or reflection response with a scanned tunable laser. However, the speed at which this signal can be acquired is typically limited by the tuning speed of the laser. The method used herein utilizes the cavity modulated background fluorescence of Si_3N_4 , which comes along with the benefit of probing the whole cavity spectrum within just the exposure time of a single spectrum, which surpasses the tuning speed and range of the lasers. Therefore, close to real time and *in situ* checks of the cavity resonances can be carried out, which is especially useful during the gas-tuning process such that the cavity tuning can be stopped at the desired frequency, e.g., in resonance. In order to evaluate the accuracy of the background method, a cross-check between the background method and resonant laser scanning is performed. Therefore, a cavity resonance with $Q \sim 2000$ is chosen, as seen in Fig. 12, and both methods yield comparable values. This proves that by using the background method, one can accurately determine the quality factors for modes with $Q \lesssim 2000$. However, with increasing Q factors one will need to re-evaluate the procedure, especially if one comes close to the resolution limit of the spectrometer.

APPENDIX I: DIPOLE ORIENTATION

In order to evaluate limiting factors of the achieved cooperativity, the angular mismatch between the SiV^- center dipole and the cavity axis is determined. Therefore, the SiV^- center fluorescence and the cavity background

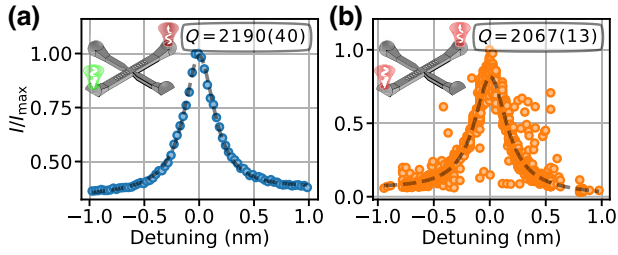


FIG. 12. (a) Background transmission spectrum for a cavity mode with a quality factor of $Q \approx 2000$, measured in accordance to the scheme described in Fig. 1(c). (b) Transmission spectrum measured by scanning a resonant laser's frequency over the same PCC resonance, as indicated by the sketch (inset). The resulting Q factor is similar to the one obtained by the method using Si_3N_4 background, hence we conclude on the background method to properly represent and map the cavity parameters as presented in Figs. 1 and 3.

signal is analyzed via a $\lambda/2$ waveplate before a polarizer prior to detection on the single-photon-counting module or in the spectrometer. The resulting polar plots are presented in Fig. 13 and reveal a mismatch of $\varphi = 66(4)^\circ$, which we identify as the main source decreasing the cooperativity by a factor of $\cos^2(\varphi) \sim 0.16$. Nanomanipulation steps to rotate NDs in order to improve the coupling can be envisioned and will yield significant improvements of optical coupling, as recently shown [30].

APPENDIX J: POWER-DEPENDENT COHERENT POPULATION TRAPPING

To evaluate the effect of power broadening in the CPT measurements, the CPT linewidth is measured at varying

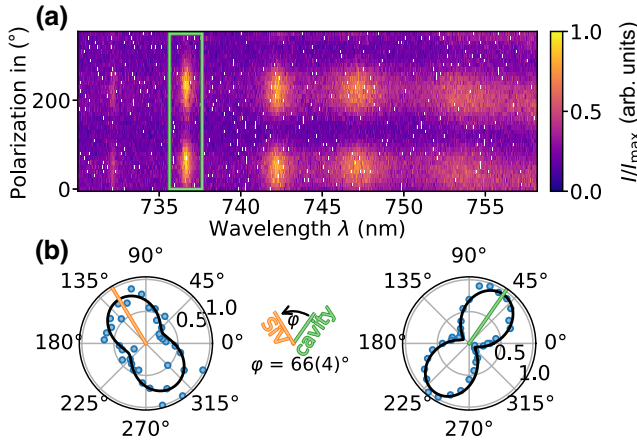


FIG. 13. (a) Normalized cavity spectra as a function of detection polarization angle. The spectra are measured as sketched in Fig. 1(c), while the green rectangle corresponds to the mode considered. (b) Detection polarization angle of the SiV^- center under investigation in the main text (orange) versus the cavity-mode polarization (green) obtained via the data of part (a), revealing an angular mismatch of $\varphi = 66(4)^\circ$.

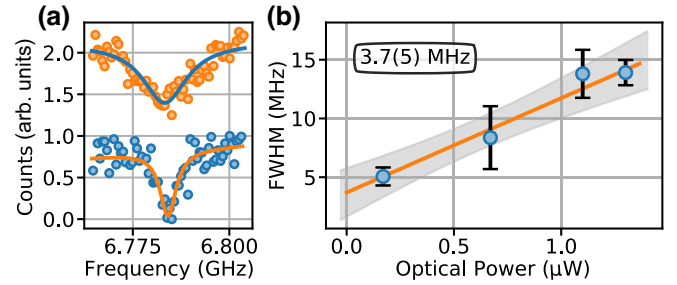


FIG. 14. (a) Exemplaric measurements to depict the effect of increased optical power, which is measured before the objective, on the resulting CPT dip width. The data is normalized and offset. (b) Linear regression of the dip width versus optical excitation powers yields a linewidth of 3.7(5) MHz, in agreement with the value of the single measurement presented in Fig. 4(f).

optical excitation powers, which leads to a broadening of the dip [Fig. 14(a)]. Extrapolating the value to zero excitation power via a linear regression [Fig. 14(b)] yields a dip width of 3.7(5) MHz, which is within the error bounds and hence in agreement of the value extracted from the single measurement discussed in Fig. 4(f) and discussed in the main text.

APPENDIX K: TUNING-INDUCED QUALITY-FACTOR CHANGE

The gas-tuning process not only allows manipulation of the cavity resonance position [Fig. 15(a)], but also had a positive effect with regards to the Q factor of the mode [Fig. 15(a)]. During cooldown the Q factor of the third mode is not significantly affected and is determined to be $Q = 940(40)$ at room temperature and $Q = 930(19)$

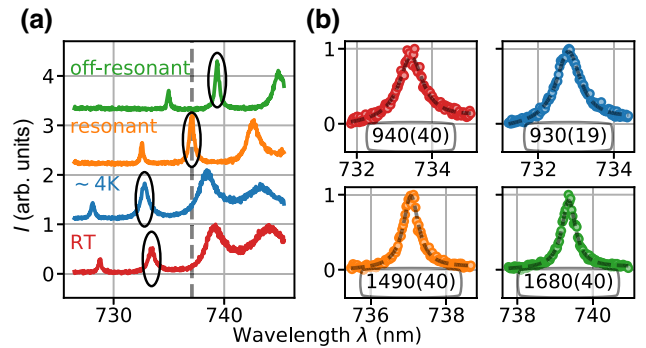


FIG. 15. (a) Cavity spectra of the PCC, measured as sketched in Fig. 1(c), at room temperature (red), at cryogenic temperature (blue), tuned into resonance with the SiV^- center (orange) and at the off-resonant detuning (green) with the resonant and off-resonant case being considered in Fig. 3. The third mode, which is under consideration in the main text, is encircled. (b) The third mode for each of the three cases considered in part (a) with annotated values of the Q factor, obtained from a Lorentzian fit (dashed line).

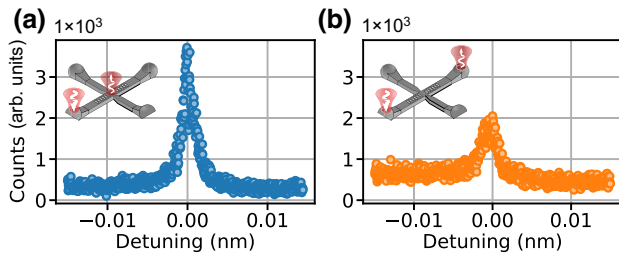


FIG. 16. (a) Exemplary PLE measurement with phonon sideband detection at the cavity’s center of an SiV^- center coupled to the cavity. Measurements are performed at zero magnetic field and in accordance to the scheme of Fig. 1(g), which is included in the inset. (b) PLE measurement of the SiV^- center, using the scheme sketched in the inset, in which the phonon sideband emission into the cavity is collected.

at cryogenic temperature. A blueshift in the resonance is originating from an increase in the Si_3N_4 refractive index, which hints towards potentially increased scattering losses after the cooldown. Tuning the third mode into resonance yields $Q = 1490(40)$ and hence an improvement by a factor of approximately 1.6, due to decreased scattering losses by a reduction in refractive-index contrast between the Si_3N_4 and the nitrogen freezing to the PCC. Further tuning increases the Q factor up to $Q = 1680(40)$ at the off-resonant position in Fig. 3(a).

APPENDIX L: PLE MEASUREMENT SCHEMES

The resonant excitation experiments carried out in the main text are measured in a PLE-type experiment in which the SiV^- center’s phonon sideband fluorescence is collected at the center of the cavity waveguide [Figs. 1(g) and 16(a)]. While it is possible to measure the phonon sideband fluorescence channeled into the cavity waveguide [Fig. 16(b)], this signal is typically weaker in comparison to detection at the cavity center, since only the higher-order modes of the cavity are resonant with the phonon sideband. Therefore, the associated enhancement of the phonon sideband is weak due to the low Q/V ratio, which cannot compensate the amount of signal that is cut out between the cavity modes. Hence, a higher signal-to-noise ratio is achievable by detecting the phonon sideband fluorescence at the center of the cavity, which explains the measurement scheme in Fig. 1(g) used throughout the main text.

-
- [1] H. J. Kimble, The quantum internet, *Nature* **453**, 1023 (2008).
 [2] S. Wehner, D. Elkouss, and R. Hanson, Quantum internet: A vision for the road ahead, *Science* **362**, eaam9288 (2018).
 [3] M. Ruf, N. H. Wan, H. Choi, D. Englund, and R. Hanson, Quantum networks based on color centers in diamond, *J. Appl. Phys.* **130**, 070901 (2021).

- [4] T. E. Northup and R. Blatt, Quantum information transfer using photons, *Nat. Photonics* **8**, 356 (2014).
 [5] L. J. Rogers, O. Wang, Y. Liu, L. Antoniuk, C. Osterkamp, V. A. Davydov, V. N. Agafonov, A. B. Filipovski, F. Jelezko, and A. Kubanek, Single SiV^- centers in low-strain nanodiamonds with bulklike spectral properties and nanomanipulation capabilities, *Phys. Rev. Appl.* **11**, 024073 (2019).
 [6] R. Waltrich, M. Klotz, V. N. Agafonov, and A. Kubanek, Two-photon interference from silicon-vacancy centers in remote nanodiamonds, *Nanophotonics* **12**, 3663 (2023).
 [7] A. Kubanek, A. P. Ovyvan, L. Antoniuk, N. Lettner, and W. H. P. Pernice, in *Progress in Nanophotonics 7*, Topics in Applied Physics, edited by T. Yatsui (Springer International Publishing, Cham, 2022) p. 123.
 [8] S. Sahoo, V. A. Davydov, V. N. Agafonov, and S. I. Bogdanov, Hybrid quantum nanophotonic devices with color centers in nanodiamonds [Invited], *Opt. Mater. Express* **13**, 191 (2023).
 [9] A. W. Schell, G. Kewes, T. Schröder, J. Wolters, T. Aichele, and O. Benson, A scanning probe-based pick-and-place procedure for assembly of integrated quantum optical hybrid devices, *Rev. Sci. Instrum.* **82**, 073709 (2011).
 [10] P. P. J. Schrinner, J. Olthaus, D. E. Reiter, and C. Schuck, Integration of diamond-based quantum emitters with nanophotonic circuits, *Nano Lett.* **20**, 8170 (2020).
 [11] K. G. Fehler, A. P. Ovyvan, L. Antoniuk, N. Lettner, N. Gruhler, V. A. Davydov, V. N. Agafonov, W. H. P. Pernice, and A. Kubanek, Purcell-enhanced emission from individual SiV^- center in nanodiamonds coupled to a Si_3N_4 -based, photonic crystal cavity, *Nanophotonics* **9**, 3655 (2020).
 [12] F. Böhm, N. Nikolay, C. Pyrlík, J. Schlegel, A. Thies, A. Wicht, G. Tränkle, and O. Benson, On-chip integration of single solid-state quantum emitters with a SiO_2 photonic platform, *New J. Phys.* **21**, 045007 (2019).
 [13] K. G. Fehler, L. Antoniuk, N. Lettner, A. P. Ovyvan, R. Waltrich, N. Gruhler, V. A. Davydov, V. N. Agafonov, W. H. P. Pernice, and A. Kubanek, Hybrid quantum photonics based on artificial atoms placed inside one hole of a photonic crystal cavity, *ACS Photonics* **8**, 2635 (2021).
 [14] K. Ngan, Y. Zhan, C. Dory, J. Vučković, and S. Sun, Quantum photonic circuits integrated with color centers in designer nanodiamonds, *Nano Lett.* **23**, 9360 (2023).
 [15] M. Klotz, K. G. Fehler, R. Waltrich, E. S. Steiger, S. Häußler, P. Reddy, L. F. Kulikova, V. A. Davydov, V. N. Agafonov, M. W. Doherty, and A. Kubanek, Prolonged orbital relaxation by locally modified phonon density of states for the SiV^- center in nanodiamonds, *Phys. Rev. Lett.* **128**, 153602 (2022).
 [16] Y.-I. Sohn, S. Meesala, B. Pingault, H. A. Atikian, J. Holzgrafe, M. Gündoğan, C. Stavarakas, M. J. Stanley, A. Sipahigil, J. Choi, M. Zhang, J. L. Pacheco, J. Abraham, E. Bielejec, M. D. Lukin, M. Atatüre, and M. Lončar, Controlling the coherence of a diamond spin qubit through its strain environment, *Nat. Commun.* **9**, 1 (2018).
 [17] S. Ritter, C. Nölleke, C. Hahn, A. Reiserer, A. Neuzner, M. Uphoff, M. Mücke, E. Figueroa, J. Bochmann, and G. Rempe, An elementary quantum network of single atoms in optical cavities, *Nature* **484**, 195 (2012).

- [18] D. J. Blumenthal, R. Heideman, D. Geuzebroek, A. Leinse, and C. Roeloffzen, Silicon nitride in silicon photonics, *Proc. IEEE* **106**, 2209 (2018).
- [19] H. Gehring, A. Eich, C. Schuck, and W. H. P. Pernice, Broadband out-of-plane coupling at visible wavelengths, *Opt. Lett.* **44**, 5089 (2019).
- [20] S. Meesala, Y.-I. Sohn, B. Pingault, L. Shao, H. A. Atikian, J. Holzgrafe, M. Gündoğan, C. Stavrakas, A. Sipahigil, C. Chia, R. Evans, M. J. Burek, M. Zhang, L. Wu, J. L. Pacheco, J. Abraham, E. Bielejec, M. D. Lukin, M. Atatüre, and M. Lončar, Strain engineering of the silicon-vacancy center in diamond, *Phys. Rev. B* **97**, 205444 (2018).
- [21] M. Ortner and L. G. Coliada Bandeira, Magpylib: A free Python package for magnetic field computation, *SoftwareX* **11**, 100466 (2020).
- [22] C. Hepp, T. Müller, V. Waselowski, J. N. Becker, B. Pingault, H. Sternschulte, D. Steinmüller-Nethl, A. Gali, J. R. Maze, M. Atatüre, and C. Becher, Electronic structure of the silicon vacancy color center in diamond, *Phys. Rev. Lett.* **112**, 036405 (2014).
- [23] T. Müller, C. Hepp, B. Pingault, E. Neu, S. Gsell, M. Schreck, H. Sternschulte, D. Steinmüller-Nethl, C. Becher, and M. Atatüre, Optical signatures of silicon-vacancy spins in diamond, *Nat. Commun.* **5**, 3328 (2014).
- [24] L. J. Rogers, K. D. Jahnke, M. H. Metsch, A. Sipahigil, J. M. Binder, T. Teraji, H. Sumiya, J. Isoya, M. D. Lukin, P. Hemmer, and F. Jelezko, All-optical initialization, readout, and coherent preparation of single silicon-vacancy spins in diamond, *Phys. Rev. Lett.* **113**, 263602 (2014).
- [25] B. Pingault, J. N. Becker, C. H. H. Schulte, C. Arend, C. Hepp, T. Godde, A. I. Tartakovskii, M. Markham, C. Becher, and M. Atatüre, All-optical formation of coherent dark states of silicon-vacancy spins in diamond, *Phys. Rev. Lett.* **113**, 263601 (2014).
- [26] A. E. Siegman, *Lasers* (University Science Books, Sausalito, CA, 1986).
- [27] S. Mosor, J. Hendrickson, B. C. Richards, J. Sweet, G. Khitrova, H. M. Gibbs, T. Yoshie, A. Scherer, O. B. Shehkin, and D. G. Deppe, Scanning a photonic crystal slab nanocavity by condensation of xenon, *Appl. Phys. Lett.* **87**, 141105 (2005).
- [28] S. Lindner, A. Bommer, A. Muzha, A. Krueger, L. Gines, S. Mandal, O. Williams, E. Londero, A. Gali, and C. Becher, Strongly inhomogeneous distribution of spectral properties of silicon-vacancy color centers in nanodiamonds, *New J. Phys.* **20**, 115002 (2018).
- [29] E. Janitz, M. K. Bhaskar, and L. Childress, Cavity quantum electrodynamics with color centers in diamond, *Optica* **7**, 1232 (2020).
- [30] N. Lettner, L. Antoniuk, A. P. Ovvyan, H. Gehring, D. Wendland, V. N. Agafonov, W. H. P. Pernice, and A. Kubanek, Controlling all degrees of freedom of the optical coupling in hybrid quantum photonics, *ACS Photonics* **11**, 696 (2024).
- [31] S. Häußler, L. Hartung, K. G. Fehler, L. Antoniuk, L. F. Kulikova, V. A. Davydov, V. N. Agafonov, F. Jelezko, and A. Kubanek, Preparing single SiV-center in nanodiamonds for external, optical coupling with access to all degrees of freedom, *New J. Phys.* **21**, 103047 (2019).
- [32] M. H. Metsch, K. Senkalla, B. Tratzmiller, J. Scheuer, M. Kern, J. Achard, A. Tallaire, M. B. Plenio, P. Siyushev, and F. Jelezko, Initialization and readout of nuclear spins via a negatively charged silicon-vacancy center in diamond, *Phys. Rev. Lett.* **122**, 190503 (2019).
- [33] D. D. Sukachev, A. Sipahigil, C. T. Nguyen, M. K. Bhaskar, R. E. Evans, F. Jelezko, and M. D. Lukin, Silicon-vacancy spin qubit in diamond: A quantum memory exceeding 10 ms with single-shot state readout, *Phys. Rev. Lett.* **119**, 223602 (2017).
- [34] M. Klotz, R. Waltrich, N. Lettner, V. N. Agafonov, and A. Kubanek, Strongly coupled spins of silicon-vacancy centers inside a nanodiamond with sub-megahertz linewidth, *Nanophotonics* (2024).
- [35] R. Debroux, C. P. Michaels, C. M. Purser, N. Wan, M. E. Trusheim, J. Arjona Martínez, R. A. Parker, A. M. Stramma, K. C. Chen, L. de Santis, E. M. Alexeev, A. C. Ferrari, D. Englund, D. A. Gangloff, and M. Atatüre, Quantum control of the tin-vacancy spin qubit in diamond, *Phys. Rev. X* **11**, 041041 (2021).
- [36] J. N. Becker, B. Pingault, D. Groß, M. Gündoğan, N. Kukharichy, M. Markham, A. Edmonds, M. Atatüre, P. Bushev, and C. Becher, All-optical control of the silicon-vacancy spin in diamond at millikelvin temperatures, *Phys. Rev. Lett.* **120**, 053603 (2018).
- [37] C. T. Nguyen, D. D. Sukachev, M. K. Bhaskar, B. Machielse, D. S. Levonian, E. N. Knall, P. Stroganov, C. Chia, M. J. Burek, R. Riedinger, H. Park, M. Lončar, and M. D. Lukin, An integrated nanophotonic quantum register based on silicon-vacancy spins in diamond, *Phys. Rev. B* **100**, 165428 (2019).
- [38] C. T. Nguyen, D. D. Sukachev, M. K. Bhaskar, B. Machielse, D. S. Levonian, E. N. Knall, P. Stroganov, R. Riedinger, H. Park, M. Lončar, and M. D. Lukin, Quantum network nodes based on diamond qubits with an efficient nanophotonic interface, *Phys. Rev. Lett.* **123**, 183602 (2019).
- [39] J. M. Binder, A. Stark, N. Tomek, J. Scheuer, F. Frank, K. D. Jahnke, C. Müller, S. Schmitt, M. H. Metsch, T. Uden, T. Gehring, A. Huck, U. L. Andersen, L. J. Rogers, and F. Jelezko, Qudi: A modular python suite for experiment control and data processing, *SoftwareX* **6**, 85 (2017).
- [40] A. Eich, T. C. Spiekermann, H. Gehring, L. Sommer, J. R. Bankwitz, P. P. J. Schrunner, J. A. Preuß, S. Michaelis de Vasconcellos, R. Bratschitsch, W. H. P. Pernice, and C. Schuck, Single-photon emission from individual nanophotonic-integrated colloidal quantum dots, *ACS Photonics* **9**, 551 (2022).
- [41] Q. Shi, B. Sontheimer, N. Nikolay, A. W. Schell, J. Fischer, A. Naber, O. Benson, and M. Wegener, Wiring up pre-characterized single-photon emitters by laser lithography, *Sci. Rep.* **6**, 31135 (2016).
- [42] A. F. Oskooi, D. Roundy, M. Ibanescu, P. Bermel, J. D. Joannopoulos, and S. G. Johnson, Meep: A flexible free-software package for electromagnetic simulations by the FDTD method, *Comput. Phys. Commun.* **181**, 687 (2010).
- [43] J. Cai, Y. Ishikawa, and K. Wada, Strain induced bandgap and refractive index variation of silicon, *Opt. Express* **21**, 7162 (2013).